Environmental Science and Pollution Research (2020) 27:16484–16495
https://doi.org/10.1007/s11356-020-08163-y

RESEARCH ARTICLE

Enhanced adsorption of antimonate by ball-milled microscale zero valent iron/pyrite composite: adsorption properties and mechanism insight

Xingyu He[1] · Xiaobo Min[1,2] · Tianyu Peng[1] · Yong Ke[1,2] · Feiping Zhao[1,2,3] · Mika Sillanpää[3] · Yunyan Wang[1,2]

Received: 7 October 2019 / Accepted: 19 February 2020 / Published online: 2 March 2020

Abstract

Ball-milling is considered as an economical and simple technology to produce novel engineered materials. The ball-milled microscale zero valent iron/pyrite composite (BM-ZVI/FeS_2) had been synthesized through ball-milling technology and applied for highly efficient sequestration of antimonate (Sb(V)) in aqueous solution. BM-ZVI/FeS_2 exhibited good Sb(V) removal efficiency ($\geq$99.18%) at initial concentration less than 100 mg Sb(V)/L. Compared to ball-milled zero valent iron (ZVI) and pyrite (FeS_2), BM-ZVI/FeS_2 exhibited extremely higher removal efficiency due to the good synergistic adsorption effect. BM-ZVI/FeS_2 showed efficient removal performance at broad pH (2.6–10.6). Moreover, the coexisting anions had negligible inhibition influence on the Sb(V) removal. The antimony mine wastewater can be efficiently remediated by BM-ZVI/FeS_2, and the residual Sb(V) concentrations ($<$ 0.96 μg/L) can meet the mandatory discharge limit in drinking water (5 μg Sb/L). Experimental and model results demonstrated that endothermic reaction and chemisorption were involved in Sb(V) removal by BM-ZVI/FeS_2. The XRD and XPS analyses confirmed that the complete corrosion of ZVI occurred on BM-ZVI/FeS_2 after Sb(V) adsorption, resulting in the enhanced Sb(V) sequestration. Mechanism analyses showed that the excellent removal performance of BM-ZVI/FeS_2 was ascribed to the high coverage of iron (hydr)oxide oxidized from ZVI. Because of the advantages of economical cost, high Sb(V) removal capacity and easy availability, BM-ZVI/FeS_2 offers a promising adsorbent for Sb(V) remediation.

Keywords Efficient sequestration · Synergistic effect · Enhanced corrosion · Sb(V) removal

Introduction

Antimony (Sb) pollution has attracted growing concern because of bioaccumulation, persistence, and carcinogenicity of Sb (Chai et al. 2016; Fei et al. 2017). Sb pollution occurs in the aqueous environment during anthropogenic and natural processes, including mining, smelting, soil runoff, and weathering (Chai et al. 2017; Liu et al. 2018; Vink 1996). In some Sb pollution areas (Sb smelting and mining area), the dissolved Sb concentration in surface water can reach up to 29.4 mg/L (He et al. 2012). The toxicity, some chemical properties, and adsorption behavior of Sb are similar to arsenic (As) (Fei et al. 2018; Li et al. 2016). In environment, many environmental factors, including dissolved organic matters and coexisting anions, affect the behavior and toxicity of Sb (He et al. 2019b; Li et al. 2019; Li et al. 2020). The European Union (EU) had listed Sb as a hazardous pollutant and set the mandatory discharge limit in drinking water (5 μg Sb/L) (Mubarak et al. 2015; Yang et al. 2017). In natural waters, Sb primarily occurs as the species of Sb(III) and Sb(V),

Responsible editor: Ioannis A. Katsoyiannis

Electronic supplementary material The online version of this article (https://doi.org/10.1007/s11356-020-08163-y) contains supplementary material, which is available to authorized users.

✉ Yong Ke
keyong000ke@csu.edu.cn

✉ Feiping Zhao
zhaofeiping1986@163.com

[1] School of Metallurgy and Environment, Central South University, Changsha 410083, Hunan, China

[2] Chinese National Engineering Research Center for Control & Treatment of Heavy Metal Pollution, Changsha 410083, Hunan, China

[3] Department of Green Chemistry, Lappeenranta University of Technology, Sammonkatu 12, 50130 Mikkeli, Finland

Sb(III) mainly exists in anoxic conditions, whereas Sb(V) dominates in oxic surface waters (Chai et al. 2017; Filella et al. 2002). It is effective to reduce Sb toxicity by the oxidation of Sb(III) to Sb(V) through biogeochemical or chemical oxidation (Leuz et al. 2006; Li et al. 2013; Skeaff et al. 2013). However, the Sb(V) oxidation product will facilitate the mobilization of Sb species in sediment (Wilson et al. 2010), it is difficult for Sb(V) removal in the practical application (Guo et al. 2009). The elevating concentration of Sb in environmental waters poses a high risk to human health and ecosystems. Antimony removal from contaminated environmental waters has received more and more concern in recent years. Thus, it is urgent to develop a simple, effective, and economical method to remove Sb(V) from water.

Several water treatment technologies such as ion exchange (Kumar et al. 2015; Yadav et al. 2010), electrochemical separation (Fu and Wang 2011; Yang et al. 2019), chemical precipitation (Luo et al. 2013), adsorption (Shao et al. 2019; Yu et al. 2019) and redox reactions (Xu et al. 2016) have been reported to remediate heavy metal/metalloid contaminated water. Among the technologies, adsorption is an attractive method due to the advantages of cost effectiveness, safety and simplicity (He et al. 2019a; Luo and Crittenden 2019; Wang et al. 2015). Recently, various adsorbents with high affinity to heavy metal ions have been reported. Recently, PVA-Fe^0 (Zhao et al. 2014), multi-walled carbon nanotubes (Xu et al. 2011), graphene (Leng et al. 2012), Fe-Mn binary oxide (Salam and Mohamed 2013), and ZCN (Luo et al. 2015) adsorbents were applied to remediate Sb(V) pollution. Despite the high Sb(V) adsorption capacities of these adsorbents, the high cost and low removal efficiency extremely limit their practical application.

The metal/metalloid or organic pollutants can be remediated by zero valent iron (ZVI), ZVI exhibited high heavy metal ions removal efficiency via mechanisms of size-exclusion, co-precipitation, and adsorption (Noubactep 2015; Puls et al. 1999; Shokes and Möller 1999). However, challenges including permeability loss and corrosive passivation still limit the application of ZVI (Guan et al. 2015; Tepong-Tsindé et al. 2015). Recently, modified technologies such as recruitment of magnetic field, bimetal alloying, and nano zero-valent iron (nZVI) strategy have been reported (Crane and Scott 2012; Cwiertny et al. 2007; Liang et al. 2014). The noble metals including Pd, Ag, and Pt in bimetal alloying are expensive and maybe lead to ecotoxicity (Crane and Scott 2012). Compared with microscale ZVI, nZVI is difficult to apply in practical application because of the complicated synthesis processes and costly precursor reagents (Crane and Scott 2012; Guan et al. 2015). The surface corrosion products (FeII/FeIII-hydroxides/oxides) of ZVI play a vital role on the heavy metal ions removal (Tepong-Tsindé et al. 2015). The method to tremendously accelerate the corrosion of mZVI can enhance contaminant sequestration by mZVI.

The challenge could be overcome through mechanochemical mixing mZVI and pyrite by mechanical ball-milling. Mechanical ball-milling is a widespread method to produce ecomaterials, such as Fe-C composites (Gao et al. 2015), bimetallic ZVI (Xu et al. 2012) and S-$mZVI^{bm}$ (Gu et al. 2017). Chemical or physical solid-solid reactions can occur during the mechanical activation process (Ke et al. 2018). Pyrite has been applied as a hopeful material for Sb (Xie et al. 2013), Cd(II) (Borah and Senapati 2006), and As (Min et al. 2017) removal. Pyrite is a cheap adsorbent source from the mineral processing plants (Han et al. 2013). Furthermore, pyrite is a good conductor of electron and electron flow is easy to cross through the Fe^0/FeS_2 interface (Gu et al. 2017; Starling et al. 1989), which will facilitate the surface corrosion of ZVI.

To combine with the advantages of mZVI and pyrite, ball milling was applied to produce ball-milled mZVI/pyrite composite (BM-ZVI/FeS_2) for Sb(V) removal. The primary objectives were to (1) synthesize and characterize BM-ZVI/FeS_2 with different mZVI:FeS_2 molar ratios; (2) investigate the influence of mZVI:FeS_2 molar ratio, contact time, initial concentration, and initial pH; (3) obtain insights into the Sb(V) removal mechanisms by BM-ZVI/FeS_2.

Materials and methods

Characterization

X-ray photoelectron spectroscopy (XPS) measurement was performed on a VG Scientific ESALAB Mark II spectrometer. The Fourier transform infrared spectroscopy (FTIR, VERTEX 70) was applied to determine the functional groups. The scanning electron microscopy (SEM) (JEOL JSM 7401) equipped with energy-dispersive spectroscopy (EDS) was applied to characterize the morphology and element distribution. The crystallinity of adsorbent was determined by X-ray powder diffraction (XRD) (Max-IIIA) with Cu Kα radiation ($\lambda = 1.5418$ Å). The inductively coupled plasma (ICP) (Agilent, USA) was applied to determine the Sb concentration.

Chemicals and materials

The pyrite (FeS_2) was originated from TongLing Nonferrous Metals Group Holding Co., Ltd. (Anhui Province, China). $KSb(OH)_6$ and iron powder (microscale zero valent iron) were purchased from Aladdin Chemistry Co., Ltd. (Shanghai, China). The mass fraction of the chemicals and materials was higher than 99%. The Milli-Q water system (Bedford, USA) was applied to purify deionized water.

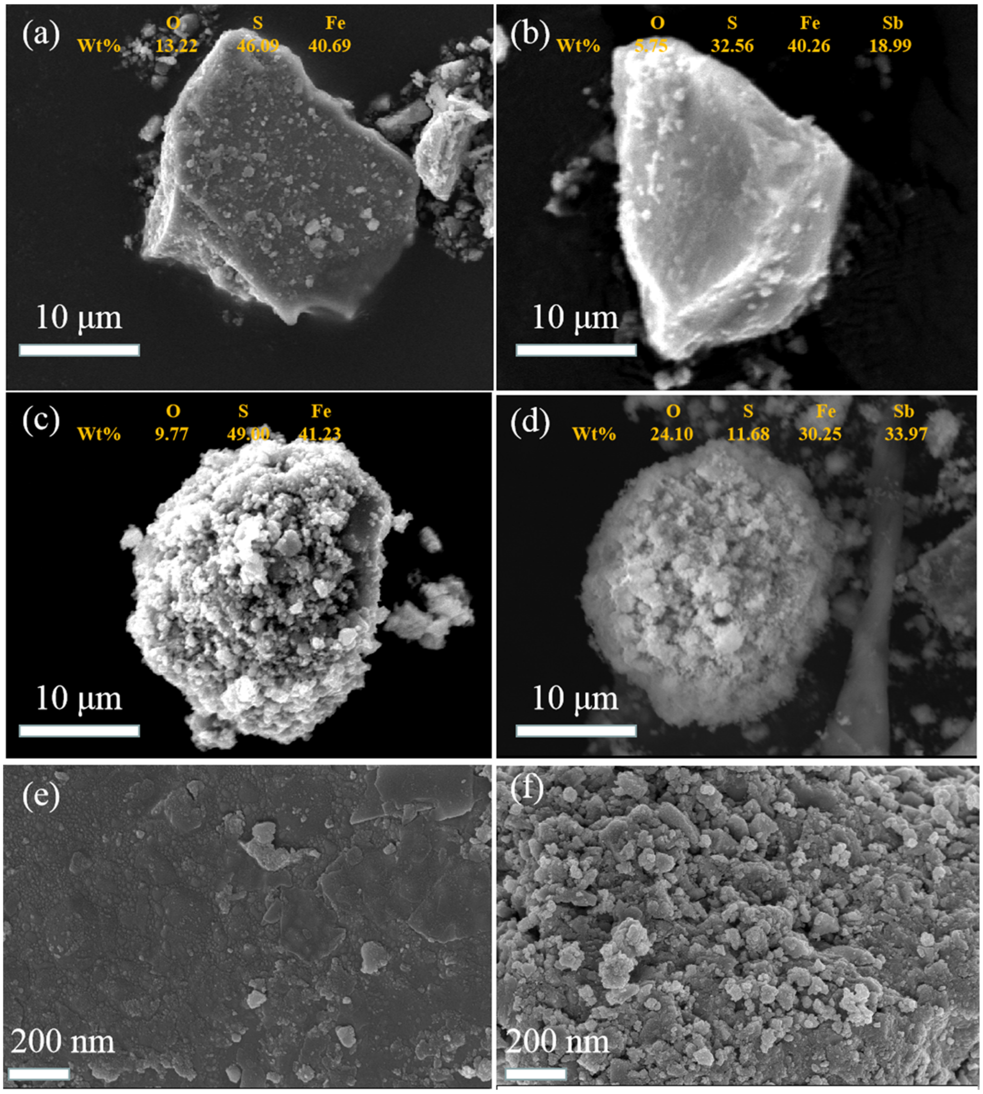

Fig. 1 SEM of FeS_2 (**a**), Sb(V)-laden FeS_2 (**b**), BM-ZVI/FeS_2 (**c**), Sb(V)-laden BM-ZVI/FeS_2 (**d**), surface morphology of FeS_2 (**e**), and BM-ZVI/FeS_2 (**f**) (the initial Sb(V) concentration used to load the adsorbents, 300 mg/L)

Preparation of BM-ZVI/FeS_2

BM-ZVI/FeS_2 was prepared in an all-round planetary ball mill machine. Briefly, 10 g of ZVI and pyrite powder mixture in various initial molar ratios was firstly placed into a 500 mL stainless pot (ball-to-material mass ratio, 20:1; 400 rpm). The Fe/FeS_2 initial molar ratios are 1:0, 9:1, 8:2, 7:3, 6:4, 5:5, 4:6, 3:7, 2:8, 1:9, and 0:1. Then, the pot was added with 400 g stainless steel balls. The determined time duration, including 4.0, 3.5, 3.0, 2.5, 2.0, 1.5, 1.0, and 0.5 h was operated to study the influence of ball-milling time.

Batch adsorption experiments

In batch Sb(V) adsorption experiments (25, 35, and 45 °C), BM-ZVI/FeS_2 (0.5 g/L) was added in Sb(V) solution (20–600 mg/L). Adsorption kinetics were investigated by adding BM-ZVI/FeS_2 or pyrite (200 mg) into Sb(V) solution (20 and 45 mg/L; 400 mL). Samples were filtered after desired reaction time. To investigate the influence of pH on Sb(V) removal performance, the pH of Sb(V) solution (50 mg/L) was adjusted with HNO_3/NaOH (0.1 M) at the range of 1–12.

The organic matters (humic acid and fulvic acid) and coexisting anions (SiO_4^{4-}, Cl^-, HCO_3^-, PO_4^{3-}, NO_3^-, and SO_4^{2-}) may affect the Sb(V) removal, and their typical concentrations in groundwater were evaluated in this study. The solution containing 100 mg/L Sb(V) was spiked with humic acid (20 mg/L), fulvic acid (20 mg/L), silicate (12, 9, 6 mg/L), bicarbonate (200, 100, 50 mg/L), phosphate (10, 5, 2 mg/L), chloride (500, 300, 100 mg/L), sulfate (500, 300, 100 mg/L), and nitrate (60, 30, 10 mg/L), respectively. After shaken for 24 h (25 °C), the residual Sb in aqueous samples was analyzed by ICP. The adsorption data analysis methods are presented in Text S1.

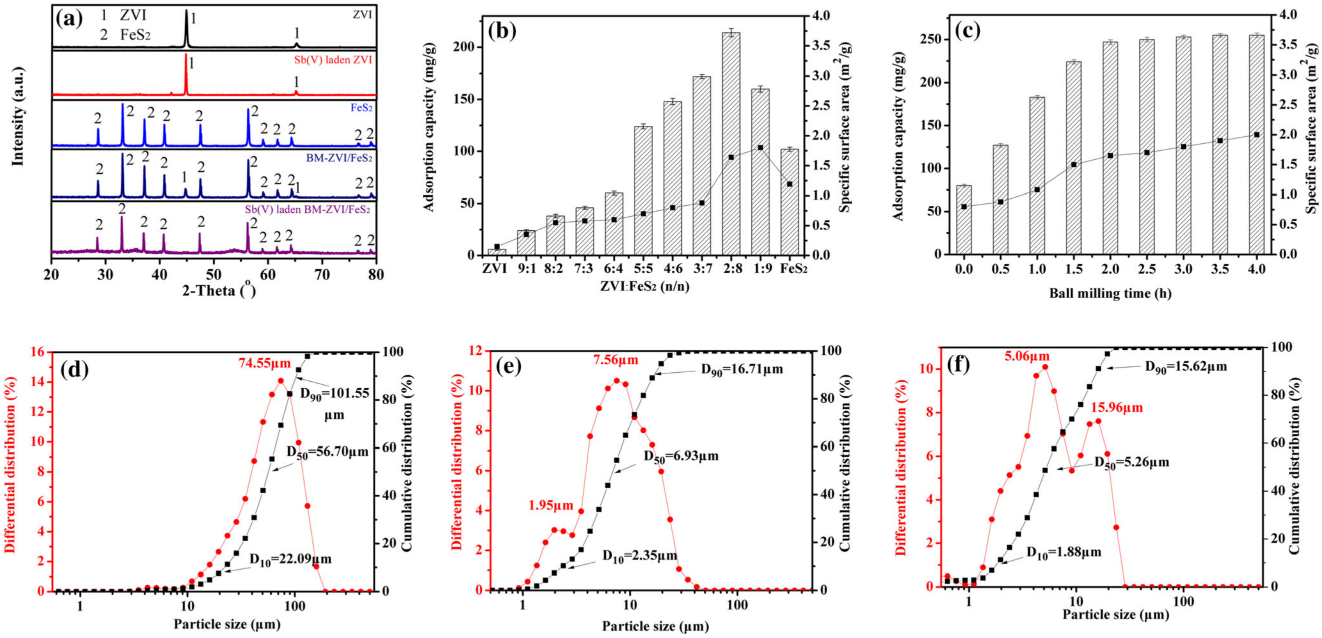

Fig. 2 XRD patterns (**a**) of BM-ZVI/FeS$_2$, Sb(V)-laden BM-ZVI/FeS$_2$, FeS$_2$, and ZVI. Effects of ZVI:FeS$_2$ molar ratios (**b**) and ball milling time (**c**) on Sb(V) adsorption capacity. Particle size distribution of ZVI (**d**), FeS$_2$ (**e**), and BM-ZVI/FeS$_2$ (**f**)

Results and discussion

Characterization

Figure 1 shows that pyrite and BM-ZVI/FeS$_2$ showed the obviously different morphology. The particles of pyrite showed irregular structure and morphology, and the surface of pyrite was very smooth (Fig. 1e). In contrast, the particles of BM-ZVI/FeS$_2$ had relatively regular structure and morphology, and a large amount of quite fine particles were distributed on BM-ZVI/FeS$_2$'s surface (Fig. 1f), leading to the extremely rough surface. The formation of rough surface and smaller particles on adsorbents can greatly improve the efficiency of contaminants remediation, which were confirmed by the previous studies (He et al. 2019a; Luo et al. 2015). The EDS analysis showed BM-ZVI/FeS$_2$ had the higher Fe mass ratio (41.23% ± 0.05) than that of pyrite (40.69% ± 0.03) due to the addition of ZVI. After Sb(V) removal, the Sb mass ratio (33.97% ± 0.04) of BM-ZVI/FeS$_2$ was greater than that of pyrite (18.99% ± 0.05), which was ascribed to the higher Sb(V) capacity of BM-ZVI/FeS$_2$. The EDS analysis showed that the O mass ratio of BM-ZVI/FeS$_2$ increased from 9.77 to 24.10%, while the O mass ratio of pyrite decreased from 13.22 to 5.75%, revealing that the corrosion of ZVI on BM-ZVI/FeS$_2$ occurred.

The crystalline structures of ZVI, Sb(V)-containing ZVI, FeS$_2$, BM-ZVI/FeS$_2$ and Sb(V)-containing BM-ZVI/FeS$_2$ were characterized by XRD. Figure 2 a shows that BM-ZVI/FeS$_2$ contained two major constituents: ZVI (iron, PDF#06-0696) and FeS$_2$ (pyrite, PDF#42-1340). For the ZVI, the characteristic peaks at 2θ of 44.6° and 65.0° are assigned to the (110) and (200) planes of ZVI, respectively. For FeS$_2$, the characteristic peaks at 2θ of 28.5°, 33.1°, 37.1°, 40.8°, 47.4°, and 56.3° are corresponded to the (111), (200), (210),

Fig. 3 Sb(V) removal efficiency (**a**) of BM-ZVI/FeS$_2$ and FeS$_2$. Influence of temperature (**b**) on Sb(V) adsorption on BM-ZVI/FeS$_2$

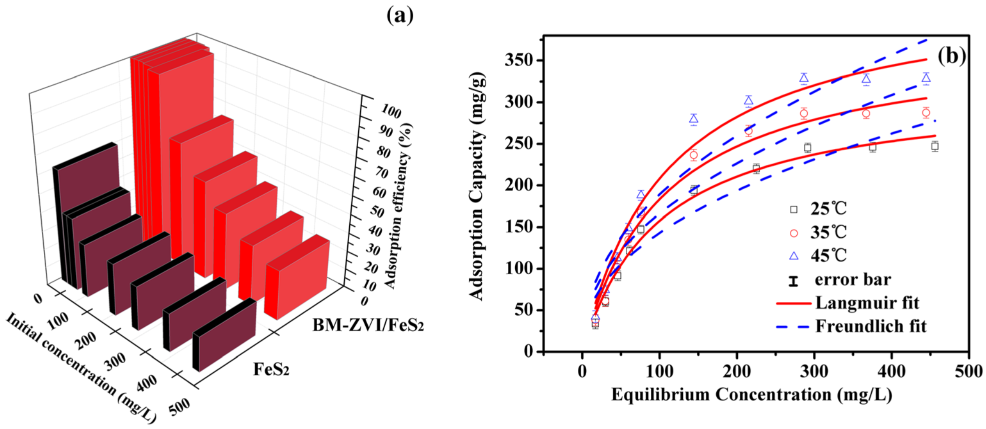

Table 1 Parameters of Freundlich and Langmuir for Sb(V) removal by BM-ZVI/FeS_2

Temp (°C)	Langmuir parameters			Freundlich parameters		
	q_m (mg/g)	K_L (L/mg)	R^2	n	K_f ($mg^{1-(1/n)}$ $L^{1/n}$/g)	R^2
25	248.1 ± 6.6	0.39 ± 0.03	0.9987	5.42 ± 0.89	96.56 ± 5.32	0.8194
35	289.0 ± 8.3	0.66 ± 0.05	0.9989	4.65 ± 0.72	102.05 ± 6.23	0.8572
45	329.0 ± 5.5	1.17 ± 0.06	0.9838	4.21 ± 0.53	111.74 ± 7.41	0.8211

(211), (220), and (311) planes of FeS_2, respectively. After preparation of BM-ZVI/FeS_2, both the characteristic peaks of FeS_2 and ZVI can be found in the XRD pattern, indicating that no obvious chemical reaction occurred between FeS_2 and ZVI. After Sb(V) adsorption, the characteristic peaks of ZVI was clearly observed in the XRD pattern of Sb(V)-laden ZVI, while for BM-ZVI/FeS_2, the characteristic peaks of ZVI disappeared, the residual peaks were observed as the characteristic peaks of FeS_2, revealing that the complete corrosion of ZVI occurred. Compared with pyrite, the intensity of primary peaks of BM-ZVI/FeS_2 was totally different. As shown in Table S1, the $I_{(200)}/I_{(220)}$, $I_{(210)}/I_{(220)}$, $I_{(211)}/I_{(220)}$, $I_{(111)}/I_{(220)}$, and $I_{(311)}/I_{(220)}$ intensity ratios increase in BM-ZVI/FeS_2. For Sb(V)-loaded BM-ZVI/FeS_2, the $I_{(200)}/I_{(220)}$, $I_{(210)}/I_{(220)}$, $I_{(211)}/I_{(220)}$, $I_{(111)}/I_{(220)}$, and $I_{(311)}/I_{(220)}$ intensity ratios decrease, implying that the crystal structure of FeS_2 may change during the milling process and Sb(V) adsorption.

Effects of ZVI:FeS_2 molar ratio and ball milling time

The effects of ZVI:FeS_2 molar ratio on Sb(V) removal performance are presented in Fig. 2b. Compared to ZVI (6.0 mg/g) and FeS_2 (102 mg/g), BM-ZVI/FeS_2 (Fe:FeS_2 = 2:8, 214 mg/g) showed 35.67 and 2.10 times higher Sb(V) removal capacities, respectively. Sb(V) uptake elevated from 6.0 to 214.0 mg/g with the elevating FeS_2 molar ratio, i.e., when Fe:FeS_2 molar ratio decreased from 1:0 to 2:8, peak removal capacity (214.0 mg/g) was reached at molar ratio of 2:8. However, further elevating the FeS_2 molar ratio to 1:9 led to 25.2% decrease in Sb(V) removal capacity, which was negatively related to the adsorbent's surface area, revealing that ZVI played vital role on Sb(V) adsorption. Compared to FeS_2, BM-ZVI/FeS_2 also had a better removal performance at the ZVI:FeS_2 molar ratio of 5:5, 4:6, and 3:7. However, the surface area of these samples was extremely low (0.70 m^2/g for ZVI:FeS_2 = 5:5, 0.80 m^2/g for ZVI:FeS_2 = 4:6, and 0.88 m^2/g for ZVI:FeS_2 = 3:7). The results further demonstrated that ZVI played a vital role on the removal process.

Figure 2 c displays that the surface area of BM-ZVI/FeS_2 elevated from 0.80 to 1.65 m^2/g when ball milling time elevated to 2.0 h. The removal capacities of BM-ZVI/FeS_2 were positively related to ball milling time. Compared to the original ZVI/FeS_2 mixture without ball milling, the BM-ZVI/FeS_2 showed 3.09 times greater Sb(V) uptake (from 80.2 to 249 mg/g). After the milling time of 2.0 h, the Sb(V) adsorption capacity of BM-ZVI/FeS_2 gradually reached equilibrium, which could be attributed to the nearly maximum gain in the surface adsorption. Considering both of preparation cost and Sb(V) adsorption capacity of BM-ZVI/FeS_2 at different ZVI:FeS_2 molar ratios, the optimum molar ratio and ball milling time were determined to be 2:8 and 2 h, respectively, which was applied in the subsequent experiments. For comparison, in this study, the ZVI and FeS_2 applied were prepared by the same ball-milling process (ball milling time, 2.0 h).

Table 2 Reported Sb(V) removal capacities (25 °C)

Adsorbent	pH	Concentration range (mg/L)	Sb(V) adsorption capacity (mg/g)	Contact time (min)	Reference
PVA-Fe^0	4–10	0–20	1.65	600	Zhao et al. (2014)
ZCN[a]	1.0–13	10-500	57.17	50	Luo et al. (2015)
GO-SCH[b]	3–10.5	0–60	158.6	> 180	Dong et al. (2015)
Iron-zirconium bimetal oxide	3–11	0–25	51.0	180	Li et al. (2012)
Activated alumina	2–11	5–75	38.0	–	Xu et al. (2001)
α-FeOOH	2–12	1.22–122	48.7	–	Guo et al. (2014)
UiO-66(NH_2)	1.5–12	10–600	105.4	20	He et al. (2017)
UiO-66	1.5–12	10–600	99.5	20	He et al. (2017)
BM-ZVI/FeS_2	1–13.1	20–600	248.1	180	This study

[a] Zirconium oxide (ZrO_2)-carbon nanofibers

[b] Graphene oxide/schwertmannite nanocomposites

Table 3 Thermodynamic parameters for Sb(V) removal by BM-ZVI/FeS_2

Adsorbent	*Temp.* (°C)	Thermodynamics parameters		
		$\triangle G_0$ (kJ/mol)	$\triangle H_0$ (kJ/mol)	$\triangle S_0$ (J/mol/K)
BM-ZVI/FeS_2	25	− 33.21 ± 0.23	48.39 ± 1.90	273.61 ± 6.13
	35	− 35.78 ± 0.28		
	45	− 40.13 ± 0.35		

Figure 2 f shows the size of BM-ZVI/FeS_2 is mainly distributed in two areas of about 5.06 and 15.96 μm. Figure 2 d and e show that ZVI and FeS_2 exhibit a median particle size (d_{50}) of 56.70 and 6.93 μm, respectively, while d_{50} of BM-ZVI/FeS_2 decrease to 5.26 μm (Fig. 2f), revealing that the ball milling of ZVI and FeS_2 can produce smaller particles of BM-ZVI/FeS_2.

Adsorption isotherms

Figure 3 a shows that FeS_2's Sb(V) removal efficiency was lower than 61.87%. In contrast, BM-ZVI/FeS_2's removal efficiency was higher than 99.18% at initial concentration less than 100 mg/L. Figure 3 b shows the adsorption isotherms of Sb(V) by BM-ZVI/FeS_2 at 45, 35, and 25 °C. BM-ZVI/FeS_2's Sb(V) uptake increased rapidly at the concentration < 100 mg/L, then increased gradually at concentration of 100–300 mg/L, and finally reached the maximum removal capacity. The equilibrium adsorption isotherm data were analyzed by Freundlich and Langmuir isotherm models. Table 1 shows that Langmuir model was better to describe the adsorption isotherm due to the higher correlation coefficients ($R^2 \geq 0.9838$), revealing the homogeneous surface adsorption of Sb(V) on the BM-ZVI/FeS_2 and uniform active sites. The BM-ZVI/FeS_2 had excellent adsorption performance of 247.0 mg Sb(V)/g (Table 2), which was larger than many reported adsorbents, such as PVA-Fe^0 (1.65 mg/g) (Zhao et al. 2014), ZCN (57.17 mg/g) (Luo et al. 2015), GO-SCH (158.0 mg/g) (Dong et al. 2015), iron-zirconium bimetal oxide (51.0 mg/g) (Li et al. 2012), activated alumina (38.0 mg/g) (Xu et al. 2001), and UiO-66 (99.5 mg/g) (He et al. 2017).

The correlation coefficients ($R^2 \geq 0.9938$) show that the equilibrium data fit well with D-R isotherm model (Fig. S1 and Table S2). According to the calculation, these free energy values (E_a) were 21.93 and 9.78 kJ/mol for BM-ZVI/FeS_2 and pyrite, respectively. The E_a value for pyrite was at the range (8–16 kJ/mol) for ion-exchange mechanism, while the E_a value for BM-ZVI/FeS_2 was higher than 16.0 kJ/mol, which revealed that chemisorption played a vital role on the Sb(V) adsorption on BM-ZVI/FeS_2 (Bulut et al. 2014).

Figure 3 b shows that the increasing temperature led to the increasing adsorption capacity. As summarized in Fig. S2 and Table 3, the adsorption process was endothermic reaction in the experimental condition, which was confirmed by positive value of ΔH^0 value (48.39 kJ/mol). The decreased degree of freedom of Sb(V) was confirmed by positive value of ΔS^0 (273.61 J/mol K). The ΔG^0 values were obtained to be − 33.21, − 35.78, and − 40.13 kJ/mol for BM-ZVI/FeS_2, indicating that adsorption of Sb(V) on BM-ZVI/FeS_2 was spontaneous adsorption reaction. The results indicated that Sb(V) adsorption on BM-ZVI/FeS_2 was spontaneous and endothermic.

Adsorption kinetics

The contact time of adsorption is critical factor for potential wastewater treatment. Figure 4 a illustrates the Sb(V) adsorption kinetics at different concentration (20 and 45 mg/L). When initial concentration of Sb(V) was 20 and 45 mg/L, the removal capacities of FeS_2 were only 22.4 and 32.2 mg/g, comparatively, the maximum adsorption capacities of BM-ZVI/FeS_2 were 39.8 and 91.4 mg/g. Additionally, the Sb(V) adsorption by FeS_2 was relatively slow. Only 52.63% of the maximum adsorption capacity was achieved after the 15 min of reaction time. While the Sb(V) adsorption by BM-ZVI/FeS_2 was rapid, the initial 15-min reaction time achieved over

Fig. 4 Adsorption kinetics (**a**) for Sb(V) adsorption on BM-ZVI/FeS_2 and FeS_2. The intraparticle diffusion model (**b**) of BM-ZVI/FeS_2 (temperature, 25 °C)

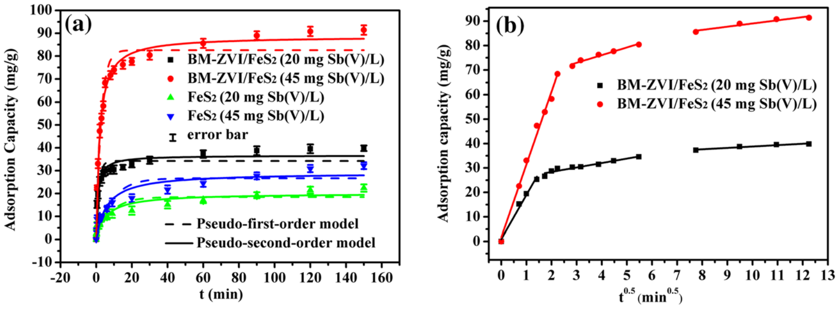

Table 4 Calculated kinetic parameters for Sb(V) removal

Adsorbent and Sb(V) concentration	Pseudo-first-order kinetics			Pseudo-second-order kinetics		
	K_1 (/min)	$q_{e.cal}$ (mg/g)	R^2	K_2 (g/mg/min)	$q_{e.cal}$ (mg/g)	R^2
BM-ZVI/FeS_2(20 mg/L)	0.69 ± 0.13	34.25 ± 1.18	0.8695	0.028 ± 0.005	36.64 ± 0.85	0.9837
BM-ZVI/FeS_2 (45 mg/L)	0.37 ± 0.04	82.61 ± 2.18	0.9458	0.006 ± 0.001	88.64 ± 1.16	0.9985
FeS_2 (20 mg/L)	0.12 ± 0.04	18.45 ± 1.38	0.8056	0.010 ± 0.002	20.08 ± 1.39	0.9804
FeS_2 (45 mg/L)	0.11 ± 0.03	26.69 ± 2.01	0.8067	0.006 ± 0.001	29.08 ± 1.05	0.9796

80.2% of the maximum adsorption capacity. The Sb(V) adsorption by BM-ZVI/FeS_2 showed the fast and slow adsorption. BM-ZVI/FeS_2 achieved 80.2% of the maximum adsorption capacity within the initial 15-min reaction time. While the adsorption time from 15 to 150 min only reached ~ 20% of the maximum adsorption capacity.

To better investigate the influence of reaction time for Sb(V) adsorption, pseudo-second-order, and pseudo-first-order models were applied to described the adsorption kinetics data. As shown in the Table 4, the better fitting was obtained for pseudo-second-order for Sb(V) adsorption, based on the higher R^2 values ($R^2 \geq 0.9796$), demonstrating that pseudo-second-order fitted the kinetics data well and Sb(V) adsorption processes of BM-ZVI/FeS_2 and FeS_2 were mainly controlled by chemisorption. The subsequent FTIR and XPS analyses confirmed the chemical reactions.

The multilinearities with three slopes are clearly shown in Fig. 4b and Fig. S3; Table S3 presented the calculated k_i and C values, and the results revealed that the adsorption processes were controlled by three steps. The first linear portion exhibited steeper q_t versus $t^{0.5}$ slope because of external mass transfer. The second linear portion showed the lower q_t versus $t^{0.5}$ slope because of pore or intraparticle diffusion rate-limiting. The third linear portion showed the lowest q_t versus $t^{0.5}$ slope because adsorption equilibrium was gradually achieved.

Influence of pH

Solution pH strongly influences the Sb(V) remediation performance of BM-ZVI/FeS_2. Figure 5 a shows that BM-ZVI/FeS_2's removal efficiency was low at pH < 1.6 (removal efficiency of 45.0%); meanwhile, the highest dissolved Fe concentration was clearly observed at pH = 1.6, revealing that large amount of adsorption sites could be destroyed at strong acidic pH. Above pH = 2.6, the Sb(V) removal efficiency of BM-ZVI/FeS_2 increased rapidly. BM-ZVI/FeS_2 had a wide pH (2.6–10.6) for Sb(V) elimination (removal efficiency > 98.0%), revealing the high affinity between Sb(V) and BM-ZVI/FeS_2. The performance of Sb(V) adsorption decreased to 82.1% at pH = 11.2 because of strong electrostatic repulsion between negative antimony species and BM-ZVI/FeS_2's negative surface. A similar Sb(V) removal tendency at the pH range was observed for FeS_2; however, the FeS_2 had a lower removal efficiency (< 69.0%) at this experiment condition (Fig. 5b). For BM-ZVI/FeS_2, the dissolved Fe concentration was relatively high at pH < 2.6 because ZVI and ferric oxide products were dissolved in strongly acid solution. The BM-ZVI/FeS_2's removal efficiency was extremely low at the pH = 1.6, indicating that the large amount of active adsorption sites on ZVI or ferric oxide products may involve in the Sb(V) removal. The dissolved Fe and S concentration in the BM-ZVI/FeS_2 mixture solution were relatively higher than that of FeS_2, which revealed that there were more corrosion products on BM-ZVI/FeS_2's surface.

Effects of coexisting anions

In practical, many environmental factors (multiple anions and organic matters) in real environmental waters may inhibit the adsorption sites on the adsorbents. As shown in Fig. S4, the organic matters (humic acid and fulvic acid) had insignificant effects on Sb(V) adsorption by BM-ZVI/FeS_2. With SiO_4^{4-}, NO_3^-, SO_4^{2-}, and Cl^- concentrations up to respective 12, 60, 500, and 500 mg/L, negligible effect was observed on Sb(V) adsorption by BM-ZVI/FeS_2 (Fig. 6a). PO_4^{3-} at 10 mg/L displayed little inhibition influence with 85% of BM-ZVI/

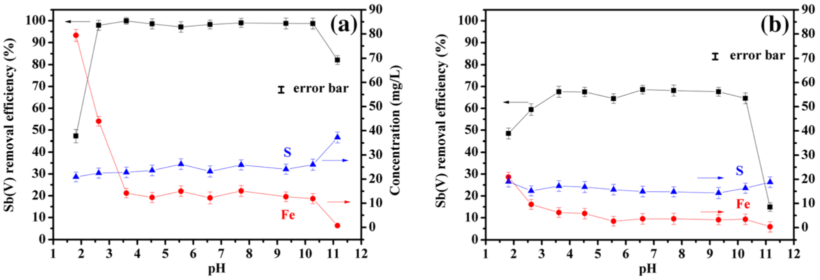

Fig. 5 Sb(V) removal efficiency of BM-ZVI/FeS_2 (**a**) and FeS_2 (**b**) at various pH values (initial Sb(V) concentration, 50 mg/L; temperature, 25 °C)

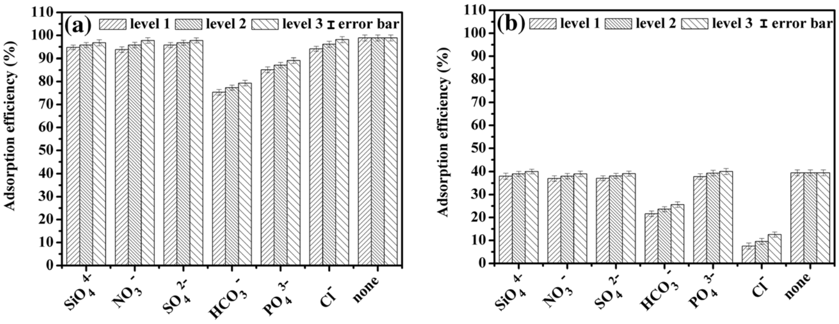

Fig. 6 Influence of coexisting anions on Sb(V) adsorption on BM-ZVI/FeS_2 (**a**) and FeS_2 (**b**) (initial Sb(V) concentration, 100 mg/L; temperature, 25 °C; the levels of anion concentration decreased in the following order: level 1 > level 2 > level 3)

FeS_2's removal efficiency for retained. HCO_3^- displayed a little inhibition influence at 200 mg/L with 74.0% of BM-ZVI/FeS_2's removal efficiency for retained. Compared with BM-ZVI/FeS_2, FeS_2 had a low removal efficiency in the Sb(V) removal. Figure 6 b shows that SiO_4^{4-}, NO_3^-, SO_4^{2-}, and PO_4^{3-} had insignificant effects on Sb(V) removal by FeS_2. HCO_3^- caused a medium inhibition, while Cl^- showed a significant inhibitory effect at concentration of 500 mg/L. Overall, BM-ZVI/FeS_2 exhibited excellent Sb(V) removal performance and showed better anti-interference ability than FeS_2. Unlike FeS_2, the coexisting anions in this study have no significant influence on Sb(V) removal by BM-ZVI/FeS_2. Thus, it is promising to employ BM-ZVI/FeS_2 to remove Sb(V) from nature waters.

The real environmental application of BM-ZVI/FeS_2

To identify the practical application performance of BM-ZVI/FeS_2, real water samples in environment (tap water, lake water and antimony mine wastewater) were investigated in this study. The lake water and tap water samples were filtered and spiked with 20 mg/L Sb(V). The antimony mine wastewater sample (pH = ~ 9.5; initial Sb concentration, 4.8 mg/L) was filtered without further treatment in this study. The BM-ZVI/FeS_2 (0.2 g) was mixed with 400 mL Sb(V) spiked tap water, lake water, and pure water, respectively; then, the liquid supernatant were collected for Sb analyses at desired adsorption times. Figure 7 a shows that the adsorption equilibrium arrived after ~ 2.5 h, the BM-ZVI/FeS_2 had large adsorption capacities of 39.5, 38.8, and 39.3 mg/g were observed for pure water, tap water, and lake water samples, respectively, while FeS_2 had the removal capacities of 18.0, 4.2, and 6.7 mg/g for pure water, tap water, and lake water samples, respectively. The Sb(V) removal capacities of FeS_2 decreased significantly in tap and lake water, unlike FeS_2, the Sb(V) adsorption capacities of BM-ZVI/FeS_2 maintained almost the same, revealing the high affinity between BM-ZVI/FeS_2 and Sb(V). Figure 7 b shows that BM-ZVI/FeS_2 exhibited high Sb removal efficiency of 99.98% in the antimony mine wastewater remediation, while FeS_2 showed low Sb removal efficiency of only 60.01%, revealing the extremely high Sb removal efficiency of BM-ZVI/FeS_2 in the practical application. Furthermore, the final Sb concentration of antimony mine wastewater treated by BM-ZVI/FeS_2 was below 0.96 μg/L, which met the mandatory discharge limit in drinking water (5 μg Sb/L). These results demonstrated that BM-ZVI/FeS_2 could be a hopeful engineered adsorbent for efficient antimony remediation in the future.

FTIR and XPS analyses

Figure S5 shows that the peak at approximate 1086 cm^{-1} was linked to the structural SO_4^{2-} anions (Han et al. 2013). The Fe-O stretching was found at 607 cm^{-1} (Bulut et al. 2014). The S-S vibrations appeared at 419 cm^{-1} (Yang et al. 2015; Yao et al. 2018). After Sb(V) removal, two peaks of SO_4^{2-} and S-S weakened slightly, indicating that the SO_4^{2-} and S-S contents might decrease after Sb(V) removal. The Sb-O antisymmetric stretching vibration at 753 cm^{-1} appeared in pyrite and BM-

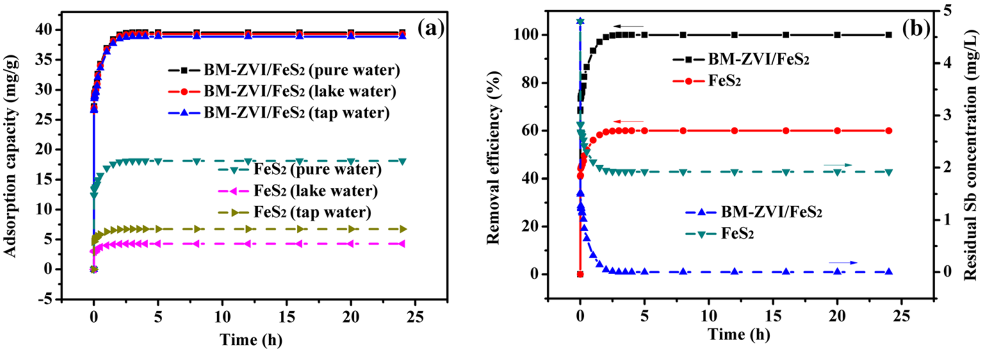

Fig. 7 Removal of Sb(V) from pure, tap, lake water (**a**) (pH, 5.6; initial concentration, 20 mg/L) and real mine drainage (**b**) (pH, ~ 9.5; initial concentration, 4.8 mg/L) by BM-ZVI/FeS_2 and FeS_2. Adsorbent dose, 0.5 g/L; shaking time, 0–24 h; temperature, 25 °C

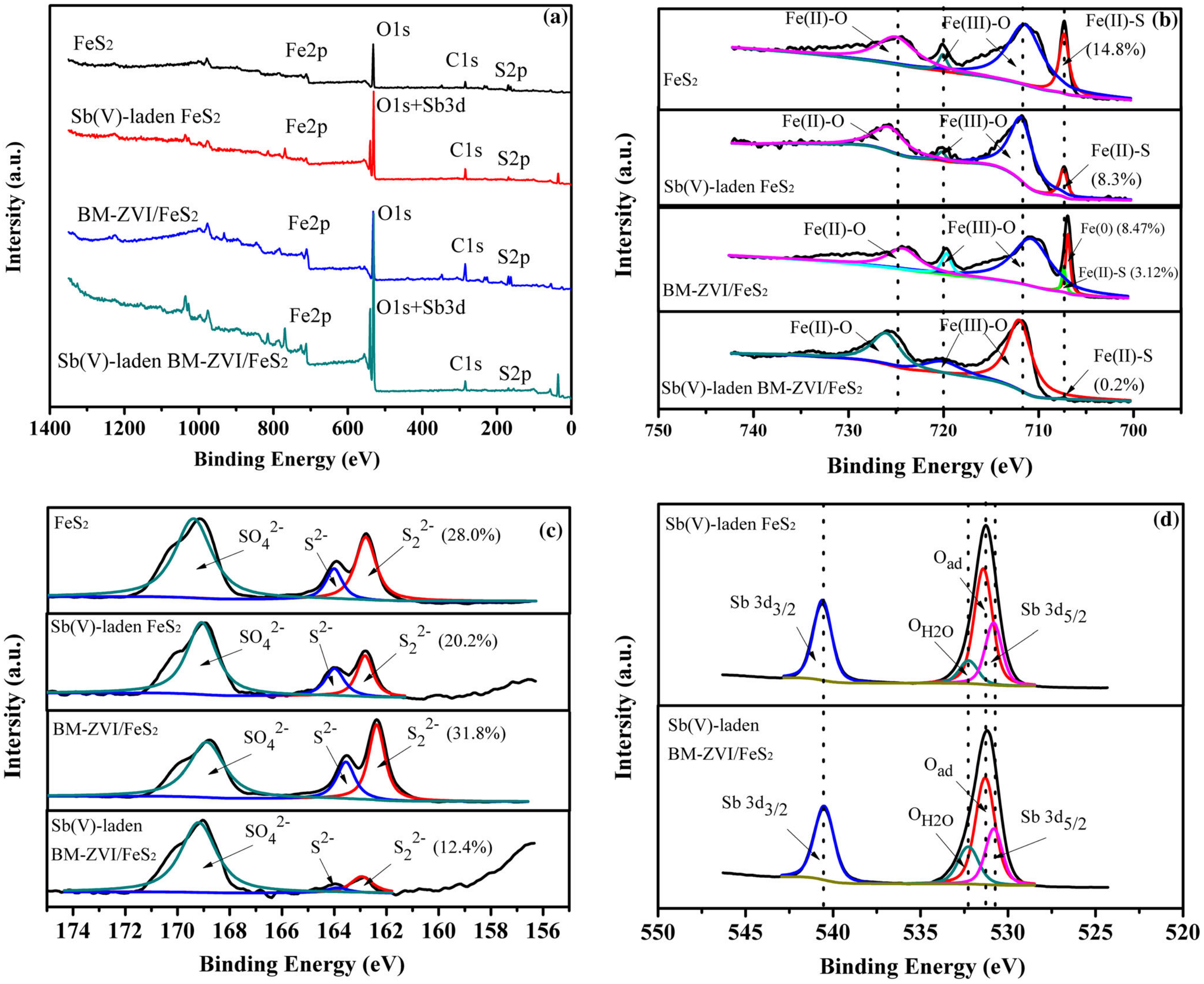

Fig. 8 XPS spectra of BM-ZVI/FeS$_2$ and FeS$_2$ before and after Sb(V) removal. **a** survey, **b** Fe 2p, **c** S 2p, and **d** O 1 s + Sb 3d

ZVI/FeS$_2$ after Sb(V) removal, revealing that the adsorbents adsorbed Sb(V) ions (Ray et al. 2009).

The XPS spectra of Sb(V)-laden pyrite, pyrite, BM-ZVI/FeS$_2$, and Sb(V)-laden BM-ZVI/FeS$_2$ are shown in Fig. 8.

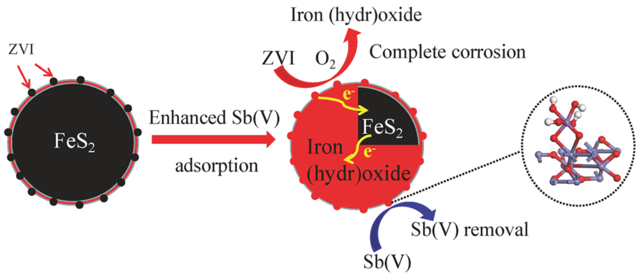

$$4Fe^{0}+3O_2+10H_2O\rightarrow 4Fe(OH)_4^{-1}+4H^{+}$$

$$4Fe^{0}+3O_2+6H_2O\rightarrow 4Fe(OH)_3$$

Fig. 9 A scheme presenting the mechanism for Sb(V) adsorption on BM-ZVI/FeS$_2$

Figure 8 a shows that the peak of Sb 3d$_{3/2}$ at 540.6 eV existed in the spectra of pyrite and BM-ZVI/FeS$_2$ after Sb(V) removal, which revealed that Sb(V) was successfully anchored on the adsorbents. The Sb 3d$_{3/2}$ binding energy of 539.7 eV of Sb(III) oxide was lower than that of the Sb(V)-laden samples (Miao et al. 2013), demonstrating that Sb(V) on the adsorbents had not been reduced. The Sb(V) content of Sb(V)-laden pyrite and Sb(V)-laden BM-ZVI/FeS$_2$ was 7.29% and 9.93%, respectively. The higher Sb(V) content of Sb(V)-laden BM-ZVI/FeS$_2$ revealed that more Sb(V) anions were anchored on Sb(V)-laden BM-ZVI/FeS$_2$. As shown in Fig. 8b, for pyrite, the Fe(II)-S, Fe(III)-O, and Fe(II)-O content were 14.8%, 56.9%, and 28.3%, respectively. Based on this result, BM-ZVI/FeS$_2$ was calculated to be composed of Fe(II)-S (3.1%), Fe(III)-O (66.2%), Fe(II)-O (22.3%), and ZVI (8.4%). Compared to pyrite, the binding energy of ZVI was clearly observed on BM-ZVI/FeS$_2$, which could be attributed to the immobilization of ZVI on the surface of pyrite during the ball milling. After Sb(V) removal by pyrite, the Fe(II)-S content decreased from 14.8 to 8.3%, while the Fe(II)-O and Fe(III)-O content increased (28.3 to 30.7% for Fe(II)-O and 56.9 to 61.0% for Fe(III)-O), indicating that Fe(II)-S was oxidized during the adsorption process. Comparatively, after Sb(V) removal by BM-ZVI/FeS_2, the peaks assigned to Fe(II)-S and ZVI were almost disappeared, while the Fe(II)-O and Fe(III)-O content increased (22.3 to 28.7% for Fe(II)-O and 66.1 to 71.1% for Fe(III)-O), revealing that the ZVI and pyritic site were oxidized and a high surface coverage of iron (hydr)oxides was covered on BM-ZVI/FeS_2 after Sb(V) adsorption (Ling et al. 2015). Various precipitated amorphous iron (hydr)oxides (FeOOH, $Fe(OH)_3$, Fe_3O_4, Fe_2O_3, $Fe(OH)_2$, etc.) were generated based on the O_2 availability. The generated iron (hydr)oxides had a high affinity towards Sb(V), resulting in the high Sb(V) removal performance of BM-ZVI/FeS_2. Figure 8 c shows that the peaks of monosulfide (S^{2-}) and disulfide (S_2^{2-}) were at 164.0 and 162.8 eV, respectively. Monosulfide was formed by breaking the S-S bonds, resulting in Fe-S bonds. The peak located at 168.4 eV indicated the presence of SO_4^{2-}, which revealed the oxidization of the surface of pyrite and BM-ZVI/FeS_2. For pyrite, the SO_4^{2-}, S^{2-}, and S_2^{2-} species contents were 61.5%, 10.6%, and 28.9%, respectively. BM-ZVI/FeS_2 was composed of SO_4^{2-} (50.7%), S^{2-} (17.6%), and S_2^{2-} (31.7%) species. After Sb(V) removal, S_2^{2-} species content of pyrite and BM-ZVI/FeS_2 decreased to respective 20.2% and 12.4%, revealing that Fe(II)-S was oxidized during the Sb(V) removal, which were consistent with the Fe $2p_{3/2}$ analyses. The Sb $3d_{3/2}$, Sb $3d_{5/2}$, O_{H2O}, and O_{ad} binding values of BM-ZVI/FeS_2 and pyrite after Sb(V) removal were almost the same (Fig. 8d), revealing that similar Sb(V) removal mechanism might occur on pyrite and BM-ZVI/FeS_2.

Mechanism analysis

The Sb(V) adsorption mechanism can be investigated by microspectroscopic characterization in combination with the results of macroscopic adsorption experiments. At the strong acid solution, pyrite's main function group is pyritic site (≡S-H) (Duan et al. 2016). As shown in Fig. 5a, at pH = 1.6, the highest dissolved Fe concentration was clearly observed while the dissolved S concentration remained nearly constant at pH < 10.2, revealing that ZVI and iron (hydr)oxides were dissolved in the solution at pH = 1.6. The Sb(V) removal efficiencies of BM-ZVI/FeS_2 and pyrite were ~ 45% and ~ 60%, respectively, revealing that FeS_2 was not only involved in the Sb(V) removal but also acting as iron (hydr)oxides and ZVI carrier. For BM-ZVI/FeS_2, when the pH increased to 2.6, the dissolved Fe concentration decreased rapidly, while the removal efficiency of BM-ZVI/FeS_2 increased to > 98%. A similar tendency was observed for Sb(V) removal by pyrite. For FeS_2, when pH increased to 2.6, the dissolved Fe concentration decreased, the removal efficiency of FeS_2 increased to ~ 73%. The enhanced corrosion of ZVI on BM-ZVI/FeS_2 led to the enhanced Sb(V) removal efficiency. The previous study had reported that pyrite is a good conductor of electrons (Starling et al. 1989). The surface of BM-ZVI/FeS_2 is composed of FeS_2/ZVI, FeS_2/Fe oxide and ZVI/Fe oxide interfaces. Electron flow is easier to transfer through the FeS_2/ZVI interface, which can enhance the oxidization of ZVI into iron hydroxides. The XPS and XRD analyses confirmed that the complete corrosion of ZVI occurred on BM-ZVI/FeS_2 after Sb(V) adsorption. The iron (hydr)oxides showed high affinity towards Sb(V) that Sb(V) primarily formed bidentate mononuclear complex on iron (hydr)oxides (Fig. 9) (Guo et al. 2014). The higher coverage of iron (hydr)oxides layer (≡Fe-OH) transformed from ZVI corrosion led to the high removal efficiency of BM-ZVI/FeS_2.

Conclusion

BM-ZVI/FeS_2 was successfully prepared by ball milling and applied for efficient Sb(V) adsorption. Compared to ZVI and FeS_2, BM-ZVI/FeS_2 exhibited higher surface area and enhanced Sb(V) adsorption ability. BM-ZVI/FeS_2 showed much larger removal efficiency than that of FeS_2. FeS_2's removal efficiency was less than 61.87%. However, the removal efficiency of BM-ZVI/FeS_2 (0.5 g/L) was larger than 99.18% (initial concentration < 100 mg Sb(V)/L). BM-ZVI/FeS_2 showed efficient Sb(V) removal performance at broad pH (2.6–10.6). BM-ZVI/FeS_2 also showed faster adsorption kinetics because of larger amounts of adsorption sites. BM-ZVI/FeS_2's Sb(V) removal processes were endothermic reaction and chemisorption, which were confirmed by experimental and model results. The XRD and XPS analyses confirmed that the complete corrosion of ZVI occurred on BM-ZVI/FeS_2 after Sb(V) adsorption, resulting in the enhanced Sb(V) sequestration. XPS analyses combined with the batch experiment results revealed that the large amount of ≡S-H and iron (hydr)oxides (≡Fe-OH) adsorption sites on BM-ZVI/FeS_2 were both involved in the Sb(V) remediation. Due to the above advantages, BM-ZVI/FeS_2 can be a hopeful engineered material for Sb(V) remediation.

Funding information The authors gratefully acknowledge National Key R&D Program of China (2018YFC1900301, 2017YFC0210402), National Science Fund for Distinguished Young Scholars (51825403), the key project of National Natural Science Foundation of China (51634010), National Natural Science Foundation of China (51904354), and Key R&D Program of Hunan Province (2019SK2281).

References

Borah D, Senapati K (2006) Adsorption of Cd(II) from aqueous solution onto pyrite. Fuel 85:1929–1934

Bulut G, Yenial Ü, Emiroğlu E, Sirkeci AA (2014) Arsenic removal from aqueous solution using pyrite. J Clean Prod 84:526–532

Chai L, Mubarak H, Yang Z, Yong W, Tang C, Mirza N (2016) Growth, photosynthesis, and defense mechanism of antimony (Sb)-contaminated Boehmeria nivea L. Environ Sci Pollut R 23:7470–7481

Chai L, Li H, Yang Z, Min X, Liao Q, Liu Y, Men S, Yan Y, Xu J (2017) Heavy metals and metalloids in the surface sediments of the Xiangjiang River, Hunan, China: distribution, contamination, and ecological risk assessment. Envrion Sci Pollut R 24:874–885

Crane RA, Scott TB (2012) Nanoscale zero-valent iron: future prospects for an emerging water treatment technology. J Hazard Mater 211–212:112–125

Cwiertny DM, Bransfield SJ, Roberts AL (2007) Influence of the oxidizing species on the reactivity of Iron-based bimetallic reductants. Environ Sci Technol 41:3734–3740

Dong S, Dou X, Mohan D, Pittman CU, Luo J (2015) Synthesis of graphene oxide/schwertmannite nanocomposites and their application in Sb(V) adsorption from water. Chem Eng J 270:205–214

Duan Y, Han DS, Batchelor B, Abdel-Wahab A (2016) Synthesis, characterization, and application of pyrite for removal of mercury. Colloids Surfaces A 490:326–335

Fei J, Min X, Wang Z, Pang Z, Liang Y, Ke Y (2017) Health and ecological risk assessment of heavy metals pollution in an antimony mining region: a case study from South China. Environ Sci Pollut R 24:27573–27586

Fei J, Wang T, Zhou Y, Wang Z, Min X, Ke Y, Hu W, Chai L (2018) Aromatic organoarsenic compounds (AOCs) occurrence and remediation methods. Chemosphere 207:665–675

Filella M, Belzile N, Chen Y (2002) Antimony in the environment: a review focused on natural waters: II. Relevant solution chemistry. Earth Sci Rev 59:265–285

Fu F, Wang Q (2011) Removal of heavy metal ions from wastewaters: a review. J Environ Manag 92:407–418

Gao J, Wang W, Rondinone AJ, He F, Liang L (2015) Degradation of Trichloroethene with a novel ball milled Fe–C Nanocomposite. J Hazard Mater 300:443–450

Gu Y, Wang B, He F, Bradley MJ, Tratnyek PG (2017) Mechanochemically sulfidated microscale zero valent iron: pathways, kinetics, mechanism, and efficiency of trichloroethylene dechlorination. Environ Sci Technol 51:12653–12662

Guan X, Sun Y, Qin H, Li J, Lo IMC, He D, Dong H (2015) The limitations of applying zero-valent iron technology in contaminants sequestration and the corresponding countermeasures: the development in zero-valent iron technology in the last two decades (1994–2014). Water Res 75:224–248

Guo X, Wu Z, He M (2009) Removal of antimony(V) and antimony(III) from drinking water by coagulation–flocculation–sedimentation (CFS). Water Res 43:4327–4335

Guo X, Wu Z, He M, Meng X, Jin X, Qiu N, Zhang J (2014) Adsorption of antimony onto iron oxyhydroxides: adsorption behavior and surface structure. J Hazard Mater 276:339–345

Han DS, Song JK, Batchelor B, Abdel-Wahab A (2013) Removal of arsenite(As(III)) and arsenate(As(V)) by synthetic pyrite (FeS_2): synthesis, effect of contact time, and sorption/desorption envelopes. J Colloid Interface Sci 392:311–318

He M, Wang X, Wu F, Fu Z (2012) Antimony pollution in China. Sci Total Environ 421–422:41–50

He X, Min X, Luo X (2017) Efficient removal of antimony (III, V) from contaminated water by amino modification of a zirconium metal–organic framework with mechanism study. J Chem Eng Data 62: 1519–1529

He X, Deng F, Shen T, Yang L, Chen D, Luo J, Luo X, Min X, Wang F (2019a) Exceptional adsorption of arsenic by zirconium metal-organic frameworks: engineering exploration and mechanism insight. J Colloid Interface Sci 539:223–234

He X, Min X, Peng T, Ke Y, Zhao F, Wang Y, Sillanpää M (2019b) Highly efficient antimonate removal from water by pyrite/hematite bi-mineral: performance and mechanism studies. J Chem Eng Data 64:5910–5919

Ke Y, Peng N, Xue K, Min X, Chai L, Pan Q, Liang Y, Xiao R, Wang Y, Tang C, Liu H (2018) Sulfidation behavior and mechanism of zinc silicate roasted with pyrite. Appl Surf Sci 435:1011–1019

Kumar N, Chaurand P, Rose J, Diels L, Bastiaens L (2015) Synergistic effects of sulfate reducing bacteria and zero valent iron on zinc removal and stability in aquifer sediment. Chem Eng J 260:83–89

Leng Y, Guo W, Su S, Yi C, Xing L (2012) Removal of antimony(III) from aqueous solution by graphene as an adsorbent. Chem Eng J 211–212:406–411

Leuz A, Hug SJ, Wehrli B, Johnson CA (2006) Iron-mediated oxidation of antimony(III) by oxygen and hydrogen peroxide compared to arsenic(III) oxidation. Environ Sci Technol 40:2565–2571

Li X, Dou X, Li J (2012) Antimony(V) removal from water by iron-zirconium bimetal oxide: performance and mechanism. J Environ Sci China 24:1197–1203

Li J, Wang Q, Zhang S, Qin D, Wang G (2013) Phylogenetic and genome analyses of antimony-oxidizing bacteria isolated from antimony mined soil. Int Biodeterior Biodegradation 76:76–80

Li Y, Min X, Chai L, Shi M, Tang C, Wang Q, Liang Y, Lei J, Liyang W (2016) Co-treatment of gypsum sludge and Pb/Zn smelting slag for the solidification of sludge containing arsenic and heavy metals. J Environ Manag 181:756–761

Li T, Song F, Zhang J, Tian S, Huang N, Xing B, Bai Y (2019) Experimental and modeling study of proton and copper binding properties onto fulvic acid fractions using spectroscopic techniques combined with two-dimensional correlation analysis. Environ Pollut:113465. https://doi.org/10.1016/j.envpol.2019.113465

Li T, Song F, Zhang J, Liu S, Xing B, Bai Y (2020) Pyrolysis characteristics of soil humic substances using TG-FTIR-MS combined with kinetic models. Sci Total Environ 698:134237

Liang L, Sun W, Guan X, Huang Y, Choi W, Bao H, Li L, Jiang Z (2014) Weak magnetic field significantly enhances selenite removal kinetics by zero valent iron. Water Res 49:371–380

Ling L, Pan B, Zhang W (2015) Removal of selenium from water with nanoscale zero-valent iron: mechanisms of intraparticle reduction of Se(IV). Water Res 71:274–281

Liu D, Min X, Ke Y, Chai L, Liang Y, Li Y, Yao L, Wang Z (2018) Co-treatment of flotation waste, neutralization sludge, and arsenic-containing gypsum sludge from copper smelting: solidification/stabilization of arsenic and heavy metals with minimal cement clinker. Envrion Sci Pollut R 25:7600–7607

Luo J, Crittenden JC (2019) Nanomaterial adsorbent design: from bench scale tests to engineering design. Environ Sci Technol 53:10537

Luo X, Wang C, Wang L, Deng F, Luo S, Tu X, Au C (2013) Nanocomposites of graphene oxide-hydrated zirconium oxide for simultaneous removal of As(III) and As(V) from water. Chem Eng J 220:98–106

Luo J, Luo X, Crittenden J, Qu J, Bai Y, Peng Y, Li J (2015) Removal of antimonite (Sb(III)) and antimonate (Sb(V)) from aqueous solution using carbon nanofibers that are decorated with zirconium oxide (ZrO_2). Environ Sci Technol 49:11115–11124

Miao Y, Han F, Pan B, Niu Y, Nie G, Lv L (2013) Antimony(V) removal from water by hydrated ferric oxides supported by calcite sand and polymeric anion exchanger. J Environ Sci-China 26:307–314

Min X, Li Y, Ke Y, Shi M, Chai L, Xue K (2017) Fe-FeS_2 adsorbent prepared with iron powder and pyrite by facile ball milling and its application for arsenic removal. Water Sci Technol 76:192–200

Mubarak H, Chai L, Mirza N, Yang Z, Pervez A, Tariq M, Shaheen S, Mahmood Q (2015) Antimony (Sb) – pollution and removal techniques – critical assessment of technologies. Toxicol Environ Chem 97:1296–1318

Noubactep C (2015) Metallic iron for environmental remediation: a review of reviews. Water Res 85:114–123

Puls RW, Paul CJ, Powell RM (1999) The application of in situ permeable reactive (zero-valent iron) barrier technology for the remediation of chromate-contaminated groundwater: a field test. Appl Genochem 14:989–1000

Ray LF, Jiří Č, Jiří S, Daniel O, Silmarilly B, Eloise CK (2009) Raman spectroscopic study of the antimonate mineral brandholzite Mg $[Sb_2(OH)_{12}]\cdot 6H_2O$. J Raman Spectrosc 40:1907–1910

Salam MA, Mohamed RM (2013) Removal of antimony (III) by multi-walled carbon nanotubes from model solution and environmental samples. Chem Eng Res Des 91:1352–1360

Shao P, Ding L, Luo J, Luo Y, You D, Zhang Q, Luo X (2019) Lattice-defect-enhanced adsorption of arsenic on zirconia nanospheres: a combined experimental and theoretical study. ACS Appl Mater Interfaces 11:29736–29745

Shokes TE, Möller G (1999) Removal of dissolved heavy metals from acid rock drainage using Iron metal. Environ Sci Technol 33:282–287

Skeaff JM, Beaudoin R, Wang R, Joyce B (2013) Transformation/dissolution examination of antimony and antimony compounds with speciation of the transformation/dissolution solutions. Integr Environ Asses 9:98–113

Starling A, Gilligan JM, Carter AHC, Foster RP, Saunders RA (1989) High-temperature hydrothermal precipitation of precious metals on the surface of pyrite. Nature 340:298

Tepong-Tsindé R, Crane R, Noubactep C, Nassi A, Ruppert H (2015) Testing metallic iron filtration systems for decentralized water treatment at pilot scale. Water-Sui 7:868–897

Vink BW (1996) Stability relations of antimony and arsenic compounds in the light of revised and extended Eh-pH diagrams. Chem Geol 130:21–30

Wang T, Zhang L, Li C, Yang W, Song T, Tang C, Meng Y, Dai S, Wang H, Chai L, Luo J (2015) Synthesis of core–shell magnetic Fe_3O_4@poly(m-phenylenediamine) particles for chromium reduction and adsorption. Environ Sci Technol 49:5654–5662

Wilson SC, Lockwood PV, Ashley PM, Tighe M (2010) The chemistry and behaviour of antimony in the soil environment with comparisons to arsenic: a critical review. Environ Pollut 158:1169–1181

Xie X, Min X, Chai L, Tang C, Liang Y, Li M, Ke Y, Chen J, Wang Y (2013) Quantitative evaluation of environmental risks of flotation tailings from hydrothermal sulfidation–flotation process. Environ Sci Pollut R 20:6050–6058

Xu Y, Ohki A, Shigeru M (2001) Adsorption and removal of antimony from aqueous solution by an activated alumina. Toxicol Environ Chem:133–144

Xu W, Wang H, Liu R, Zhao X, Qu J (2011) The mechanism of antimony(III) removal and its reactions on the surfaces of Fe–Mn binary oxide. J Colloid Interface Sci 363:320–326

Xu F, Deng S, Xu J, Zhang W, Wu M, Wang B, Huang J, Yu G (2012) Highly active and stable Ni–Fe bimetal prepared by ball milling for catalytic hydrodechlorination of 4-chlorophenol. Environ Sci Technol 46:4576–4582

Xu C, Zhang B, Wang Y, Shao Q, Zhou W, Fan D, Bandstra JZ, Shi Z, Tratnyek PG (2016) Effects of sulfidation, magnetization, and oxygenation on azo dye reduction by zerovalent iron. Environ Sci Technol 50:11879–11887

Yadav AK, Kumar N, Sreekrishnan TR, Satya S, Bishnoi NR (2010) Removal of chromium and nickel from aqueous solution in constructed wetland: mass balance, adsorption–desorption and FTIR study. Chem Eng J 160:122–128

Yang Z, Liu L, Chai L, Liao Y, Yao W, Xiao R (2015) Arsenic immobilization in the contaminated soil using poorly crystalline Fe-oxyhydroxy sulfate. Environ Sci Pollut R 22:12624–12632

Yang Z, Wu Z, Liao Y, Liao Q, Yang W, Chai L (2017) Combination of microbial oxidation and biogenic schwertmannite immobilization: a potential remediation for highly arsenic-contaminated soil. Chemosphere 181:1–8

Yang L, Yi G, Hou Y, Cheng H, Luo X, Pavlostathis SG, Luo S, Wang A (2019) Building electrode with three-dimensional macroporous interface from biocompatible polypyrrole and conductive graphene nanosheets to achieve highly efficient microbial electrocatalysis. Biosens Bioelectron 141:111444

Yao L, Min X, Xu H, Ke Y, Liang Y, Yang K (2018) Hydrothermal treatment of arsenic sulfide residues from arsenic-bearing acid wastewater. Int J Env Res Pub He 15:1863

Yu H, Shao P, Fang L, Pei J, Ding L, Pavlostathis SG, Luo X (2019) Palladium ion-imprinted polymers with PHEMA polymer brushes: role of grafting polymerization degree in anti-interference. Chem Eng J 359:176–185

Zhao X, Dou X, Mohan D, Pittman CU, Ok YS, Jin X (2014) Antimonate and antimonite adsorption by a polyvinyl alcohol-stabilized granular adsorbent containing nanoscale zero-valent iron. Chem Eng J 247:250–257